AIAA JOURNAL
Vol. 43, No. 3, March 2005

Development of Megahertz-Rate Planar Doppler Velocimetry for High-Speed Flows

Brian S. Thurow,* Naibo Jiang,* Walter R. Lempert,† and Mo Samimy‡
The Ohio State University, Columbus, Ohio 43210

A pulse burst laser and either one or two high-speed charge-coupled-device cameras were used to perform one-component time-resolved planar-Doppler-velocimetry (PDV) measurements in a rectangular Mach 2.0 jet. The measurements were carried out on a streamwise plane passing through the jet centerline and covering approximately 6–12 jet heights downstream of the jet exit. The pulse burst laser operated at 0.532-μm wavelength and produced 28 pulses at 250 kHz with approximately 9 mJ/pulse energy. Velocity image sequences consisting of 28 frames showed dynamics of the velocity field over a time span of 108 μs (approximately 4.5 convective timescales). A typical sequence of images is presented, which demonstrates the process of entrainment of low-speed fluid into the high-speed region of the jet. Mean and standard deviation statistics of the velocity calculations produced expected trends and showed good agreement between the single- and two-camera experiments. An error analysis revealed speckle as the predominant source of noise, as in a conventional PDV technique. At a transmission ratio of 0.5, the estimated total error is 13 m/s for the single-camera experiment and 15 m/s for the two-camera experiment.

I. Introduction

PLANAR Doppler velocimetry is a powerful optical diagnostic technique that can be used to measure all three components of instantaneous velocity over a two-dimensional plane within a flowfield with high spatial resolution. This is accomplished by using an atomic or molecular vapor filter to measure the frequency shift of light as it is scattered by particles contained in the flowfield. The Doppler shift Δf_d is in turn related to the fluid velocity by the simple expression

$$\Delta f_d = [(\boldsymbol{s} - \boldsymbol{o})/\lambda] \cdot \boldsymbol{V} \tag{1}$$

where $\boldsymbol{s}$ is the unit vector in the direction of the scattered light, $\boldsymbol{o}$ is the unit vector in the direction of the incident laser light, λ is the wavelength of the light, and $\boldsymbol{V}$ is the velocity vector of the flow.

The concept of measuring fluid velocity by means of the Doppler shift was originally utilized by Cummins et al.[1] (1964) and Yeh and Cummins[2] (1964), on which the point measurement technique now known as laser Doppler velocimetry (LDV) is based.[3] Subsequently, Komine and Brosnan[4] and Meyers and Komine[5] developed a planar velocimetry method referred to as Doppler global velocimetry, where a molecular filter was used to measure the Doppler shift. This approach is conceptually similar to what is now known as filtered Rayleigh scattering.[6] Since these original works, the technique has been further developed by numerous research groups including Elliott et al.,[7] Arnette et al.,[8] McKenzie,[9] Smith et al.,[10] Clancy and Samimy,[11] et al.,[12] Beutner et al.,[13] Mosedale et al.,[14] and Crafton et al.[15] In the course of development, many researchers began using the term planar Doppler velocimetry (PDV) to describe the technique. This term will subsequently be used in this work.

Today, a typical one-component PDV instrument utilizes a pulsed injection-seeded Nd:YAG laser, one or two scientific grade charge-coupled-device (CCD) cameras, and a molecular iodine filter. The laser is used to illuminate a plane of the flow with narrow spectral linewidth light. The Doppler-shifted scattered light is then split into two paths using a beamsplitter and imaged onto the camera(s). In this manner the absolute absorption of scattered light, as it passes through an iodine cell placed in one of the beam paths, is measured at every spatial location within the object plane. For scattering by relatively large (as compared to molecular dimension) particles, this absorption is a function of particle velocity only. Accurate calibration and image mapping algorithms have been developed with the result that velocity accuracies of approximately 1–2 m/s is now achievable. More details concerning the history of PDV, the art of its application, and recent advances can be found in comprehensive review papers by Elliott and Beutner[16] and Samimy and Wernet.[17]

However, a current limitation, common to any planar velocity measurement technique, is its inability to acquire time-correlated sets of velocity data in high-speed flows. Typical commercially available high-pulse-energy pulsed Nd:YAG lasers are limited to repetition rates of the order of 10–30 Hz and only recently have high-speed digital cameras become commercially available. These factors have limited PDV to instantaneous and ensemble-averaged flow measurements. The ability to capture time-resolved PDV measurements, however, has the potential to reveal characteristics of the dynamics of high-speed flows that currently can only be conjectured. This information could lead to new advances in the understanding and manipulation of high-speed flows and their respective applications.

Recently, a pulse burst laser that can achieve pulse burst repetition rates of up to 1 MHz was developed.[18–20] The laser has been used extensively in conjunction with a high-speed CCD camera to produce qualitative flow visualizations and quantitative convective velocity measurements by Thurow et al.[20,21] In terms of PDV, a very preliminary proof-of-concept work by Thurow et al.[22] showed the feasibility of using the pulse burst laser and available high-speed cameras to obtain PDV velocity data. A subsequent work[23] expanded upon this earlier work and identified areas of concern about the application of the pulse burst laser to a PDV system. In the current work, some of these concerns have been addressed, and a much improved set of one-component megahertz-rate PDV data has been produced. In addition, error estimates are also made, which indicate the potential expansion of the megahertz-rate PDV to two- and three-component systems.

Presented as Paper 2004-0023 at the AIAA 42nd Aerospace Sciences Meeting, Reno, NV, 5–9 January 2004; received 20 January 2004; accepted for publication 12 May 2004.

*Graduate Student, Gas Dynamics and Turbulence Laboratory, Department of Mechanical Engineering. Member AIAA.

†Associate Professor, Gas Dynamics and Turbulence Laboratory, Department of Mechanical Engineering. Associate Fellow AIAA.

‡Professor, Gas Dynamics and Turbulence Laboratory, Department of Mechanical Engineering; Samimy.1@osu.edu. Associate Fellow AIAA.

II. Experimental Apparatus and Arrangement

A. Experimental Apparatus

The pulse burst laser is a second-generation Nd:YAG laser system with the ability to produce a variable number of short-duration (~10-ns) laser pulses at repetition rates up to 1 MHz. The system has been described previously by Lempert et al.,[18] Wu et al.,[19] and Thurow et al.[20,21] In the experiments described herein, a typical burst consists of 28 pulses separated in time by 4 μs each (250-kHz repetition rate) and with an average energy of 9 mJ/pulse at 0.532 μm. In general, pulse energies are not uniform over an entire burst of pulses. The distribution is shown in Fig. 1. More uniform distributions of pulse energies are attainable by adding individual delays to each of the five laser amplifiers but generally at the sacrifice of overall power.

The pulse burst laser frequency characteristics are determined by the master oscillator, which is a Lightwave Electronics diode-pumped continuous-wave (cw) nonplanar ring laser operating at 1.064 μm. The cw laser outputs a single longitudinal mode with bandwidth less than 5 kHz. The pulse burst is formed by "slicing" the cw beam, using two Pockels cells, and subsequent amplification in a chain of five Nd:YAG laser rod amplifiers. The output pulses are Fourier transform limited and have an estimated bandwidth of approximately 65 MHz for a measured pulse duration of 6.9 ns at 1.064 μm. The center frequency is determined by the temperature-dependent index of refraction and geometry of the Nd:YAG crystal within the cw laser and is tuned by adjusting the voltage input to a thermoelectric cooler in contact with the crystal. Across the entire voltage range of -10–$+10$ V, the laser frequency experiences seven mode hops. In between mode hops, the tuning coefficient varies between 8.6 and 10.1 GHz/V. For the settings used in the current experiments, the tuning coefficient was measured to be 8.62 GHz/V.

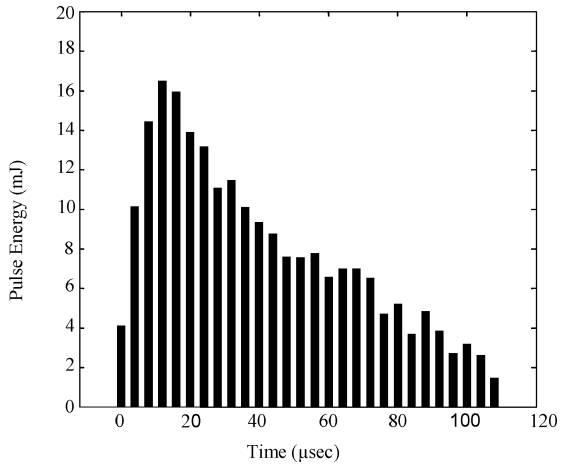

Fig. 1 Distribution of laser energy among 28 pulse burst at 532 nm.

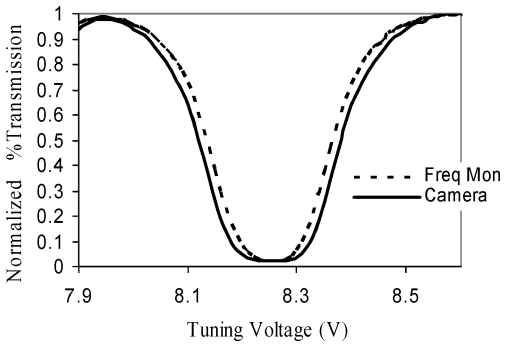

Fig. 2 Transmission ratio of iodine molecular filters vs laser tuning voltage.

Unlike typical pulsed Nd:YAG lasers whose frequency characteristics are achieved through injection seeding, the pulse burst laser is essentially an amplified seed laser. In conventional pulsed Nd:YAG lasers, cavity mirror dithering must be used to match the frequency of the linear oscillator with the frequency of the injection seed laser. This leads to pulse-to-pulse fluctuations in laser frequency on the order of 20 MHz. In addition, a small frequency variation across the beam profile, termed frequency chirp, can arise from the use of linear oscillators. The pulse burst laser, lacking a linear oscillator or injection seeder, should not experience either of these effects. Measurements confirming this will be discussed shortly.

Two iodine molecular filters were used in these experiments: one for determining the absorption of scattered light and the other for monitoring the frequency of the excitation laser. The cylindrical cells have dimensions 10 cm (length) $\times$ 10 cm (diameter). The iodine cell for frequency monitoring was prepared with an iodine partial pressure of 4.28 torr and pressure broadened with nitrogen at 41 torr, while the other cell was prepared with 3.05 torr iodine and 30.0 torr nitrogen. Electric heating tape surrounds the cells and is used to keep the cell's temperature at approximately 130 °C. The cells were calibrated with the pulse burst laser before and during the experiments using the frequency monitoring system described in the next section. Figure 2 is a graph of their calibration about the absorption well located at 18789.28 cm^{-1}.

A laser frequency monitoring system was used to measure and calibrate the laser frequency before, during, and after experimental runs. The system was modeled after the monitoring systems described by Mosedale et al.[14] and Crafton et al.[15] and used a modified version of the software described by Crafton et al.[15] A low-energy (approximately 0.5%) portion of the beam is sampled from the main beam using a thin-film polarizer and a half-wave plate. The beam is expanded to ~20 mm diam, where it enters the system shown in Fig. 3. One-half of the beam is passed through an iodine filter, focused onto a flash-opal diffuser and sampled by a high-speed photodetector. The other half of the beam is likewise focused onto a diffuser and sampled by a photodetector. For calibration of multiple iodine cells, a third arm (not shown) was added to the system using an additional beam-splitter, diffuser, and photodiode. Stanford Research Systems gated integrators were used to sample the photodiodes output over an approximately 50-ns window timed to coincide with the first laser pulse within a burst of pulses. The resulting signal

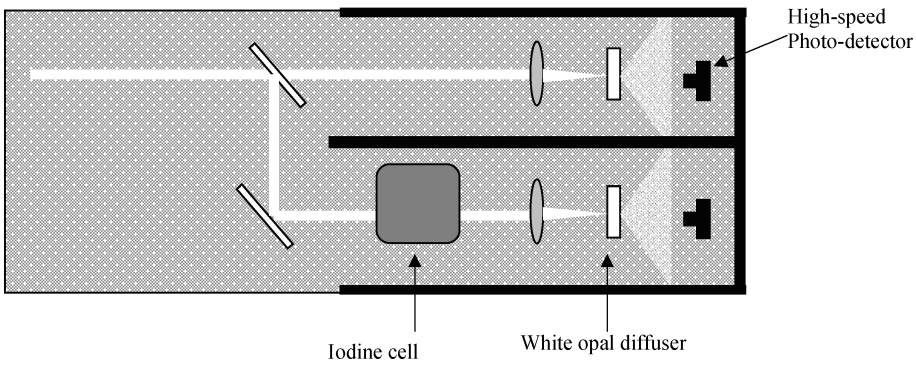

Fig. 3 Schematic of frequency monitoring system.

Table 1 Summary of high-speed camera attributes

Attribute	PSI camera 1	PSI camera 2
No. of frames	28	32
Max. frame rate	1×10^6	1×10^6
Resolution	80×160	90×180
Pixel size	115 μm	92 μm
Fill factor	47.6 %	34%
Pixel noise, rms	3 counts	~20 counts
Saturation level	17,000 counts	12,400 counts

(filtered) and reference (unfiltered) measurements were then ratioed to determine the amount of absorption produced by the iodine cell. Figure 2 was obtained by scanning the tuning voltage of the pulse burst laser from 7.9 to 8.6 V in 0.01-V increments and averaging 100 measurements for each point.

System accuracy was estimated by tuning the laser to various locations within the iodine cell's filter profile and monitoring fluctuations of the measured transmission ratio. Regardless of the laser frequency's set point, the measured transmission ratio fluctuated by approximately 3% of its set value. If the fluctuations were entirely caused by frequency jitter, a 3% fluctuation at a transmission ratio of 0.5 would correspond to a frequency fluctuation of 12 MHz. The fact that the fluctuations remained at a constant 3% at all points in the frequency profile, however, indicates that these fluctuations are not caused by frequency jitter, but rather by noise within the frequency monitoring system. At the very least, these measurements indicate that the pulse burst laser frequency is stable to within the measurement accuracy of 12 MHz.

By taking measurements over long periods of time, the frequency drift of the laser was found to be approximately 50 MHz/h. In an earlier work,[23] the frequency drift was quoted to be as high as 800 MHz/h, and it was speculated that the incorporation of a phase conjugate mirror into the laser system was the cause. The source of this frequency drift, however, has since been determined to be inadequate cooling of the cw laser head. A small fan has been integrated into the pulse burst laser, and frequency drift is no longer considered a problem. In light of these results, the frequency monitoring system was used during experiments to monitor laser frequency drift but not the instantaneous laser frequency.

Two cameras were used in the current set of experiments, both manufactured by Princeton Scientific Instruments; cameras 1 and 2. Camera 2 is on loan from the Air Force Research Laboratory. The cameras have similar attributes, which are summarized in Table 1. High frame rates are achieved by shifting charge produced at each pixel location to an array of individual memory modules contained next to each pixel location. To preserve a moderate fill factor and because of the short exposure times associated with high-speed imaging, the pixels are quite large (approximately 100 μm). This attribute is particularly suitable for megahertz-rate PDV as it increases image intensity and reduces speckle noise considerably. The CCD chip on camera 1 is of high quality with only some minor defects. Based on flat-field correction measurements to be discussed in the next section, the sensitivity of each pixel to incident light is preserved over all 28 frames. Camera 2's CCD chip, however, is of lesser quality and has significant defects. These defects take the form of horizontal lines of "dead" pixels that must be accounted for in the postprocessing PDV steps. In addition, the locations of the dead pixels can move from one image to the next, further compounding the problem.

B. Experimental Arrangement

Figure 4 is a schematic of the two-camera, one-component PDV system. Scattered light from the flowfield is split into two using a beamsplitter and imaged onto each high-speed camera with an f/# 2.8, 80–200-mm-focal-length zoom lens. To remove any dependence of the beam-splitter's properties on incident polarization, a polarizer is placed in the path. The iodine cell is placed in front of camera 1 to acquire the signal image, and camera 2 is used to acquire the reference image. A neutral-density filter of 0.6 strength is placed in front of the reference camera to provide a better balance

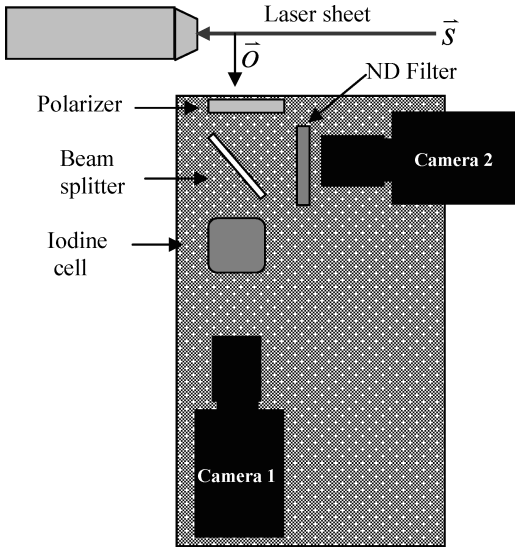

Fig. 4 Schematic of two-camera PDV system.

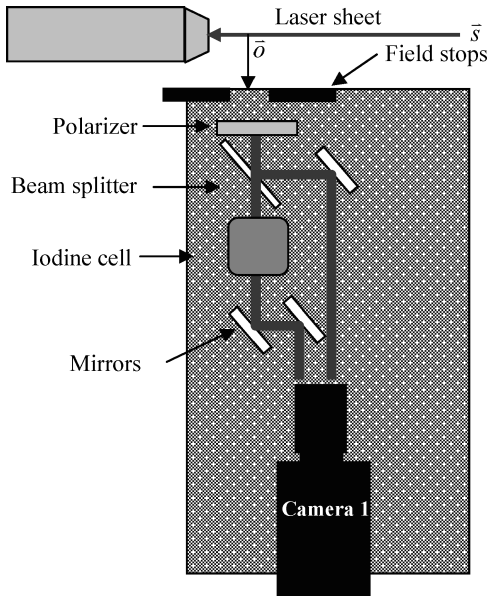

Fig. 5 Schematic of single-camera PDV system.

of image intensity between the signal and reference cameras. The two lenses were set to a focal length of approximately 135 mm and focused to image a flowfield from 6.4 jet heights (x/h) to 13.2 x/h downstream of the rectangular nozzle exit yielding a resolution of 0.48×0.48 mm/pixel.

Because of the high cost of high-speed CCD cameras and the desire to move to a two-component megahertz-rate PDV system in the future, significant effort was made to obtain PDV results using a single camera. To achieve this goal, a splitter/recombiner system using 50.8-mm square mirrors was used to acquire both filtered and unfiltered images onto a single CCD chip. A schematic of this system is shown in Fig. 5 and is based on a configuration originally developed by McKenzie,[9] Smith et al.,[10] and Clancy and Samimy.[11] The 2:1 aspect ratio of the chip is especially conducive for this arrangement. A typical problem with this type of arrangement, however, is the inherent image overlap that occurs between the signal and reference images as they are imaged onto the same, almost square, CCD chip. Typically, this can cause a significant portion of the CCD chip resolution to be unusable. This problem was circumvented by the strategic placing of two field stops (solid pieces of aluminum). These field stops physically blocked any scattered light outside of the desired imaging region from entering into the splitter/recombiner system. The camera lens and mirrors were set to image the jet flow

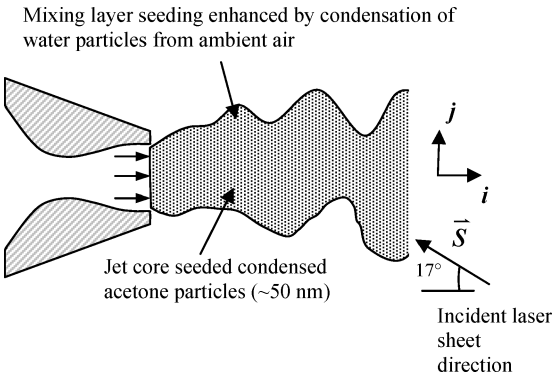

Fig. 6 Side view of flowfield with incident laser sheet.

from approximately 8.0 to 12.0 x/h downstream of the nozzle exit, yielding a resolution of 0.67×0.67 mm/pixel.

The flowfield under investigation in the current study is a Mach 2.0 rectangular jet with exit dimensions of 38.1×12.7 mm. Seed particles are introduced into the jet by the introduction of a small amount of acetone (approximately 0.4% by mass) about 15 m upstream of the rectangular nozzle, which evaporates prior to reaching the nozzle plenum. Upon expansion to supersonic velocity the gas phase acetone condenses into tiny particles estimated to be on the order 50 nm (Ref. 24). Seeding of the jet is further enhanced in the mixing layer as water vapor from the ambient air, entrained into the jet, also condenses upon mixing with the cold jet core fluid. The presence of condensed acetone also serves as a nucleation point for the water to condense.

As shown in Fig. 6, the laser sheet is introduced at a 17-deg angle with respect to the jet axis and illuminates a streamwise plane of the flow coinciding with the jet center line. Figure 5 is a top view of the system and does not reflect this angle of propagation, whereas Fig. 6 is a side view. The camera system is located perpendicular to the laser sheet. The resultant velocity vector sensitivity is in the $0.68\,\boldsymbol{i} - 0.20\,\boldsymbol{j} + 0.71\,\boldsymbol{k}$ direction with $\boldsymbol{i}$ being the streamwise component and $\boldsymbol{j}$ the cross-stream component as defined in Fig. 6; $\boldsymbol{k}$ is the out-of-plane unit vector. Viewing a streamwise plane of the flow is the most conducive for following large-scale turbulence structures as they convect predominantly in the streamwise direction. Measurement of a component of velocity entirely within the visualized plane is not possible with only a one-component PDV system.

III. Data Reduction

Variations exist among different researchers as to the specific method used to reduce the acquired signal and reference images to a velocity measurement. Regardless of preference, the main steps in any PDV experiment consist of image alignment, flat-field correction, and conversion to velocity. In this work, image alignment and flat-field calibrations were performed using images of the jet acquired with the laser tuned to full transmission through the iodine filter.

The conventional approach used for image alignment/mapping is to take an image of a dot card where the center of each dot can be used as a "tie" point between the two images. Determining the locations of multiple dots in the images allows for a function to be determined that can be used to map all images to a common grid. For optimal results, this technique requires precise alignment of the dot-card plane with the laser-sheet plane. This technique was used with moderate success in the current experiments. However, an alternative method that is believed to be just as accurate, but more reliable and convenient than the conventional dot-card approach was developed. This method is detailed next.

During data acquisition, the laser's frequency was set for maximum transmission through the iodine cell (8.60 V in Fig. 2), and the jet was operated overexpanded (p_o approximately 50 psi below its ideally expanded operation condition of approximately 100 psig). Operation of the jet in this manner produces a shock-cell pattern starting from the nozzle exit, which should diffuse the flow to subsonic velocities within a few jet exit heights. Thus, a thicker mixing layer with lower velocities fills the imaged region approximately 10 nozzle exit heights downstream of the nozzle exit. Pitot measurements showed the velocity in this region to be approximately half of that of an ideally expanded jet. Moving the jet upstream so that the low-velocity subsonic region was imaged was not an option because of the fixed jet stand upon which the nozzle was attached.

As the laser was tuned to the relatively flat, full transmission portion of the filter profile, both the signal and reference images should be nearly identical. An image transformation can then be determined to map the two nearly identical images to a common plane. A computer algorithm was developed to match flow features between the signal and reference image to determine this transformation. The algorithm works as follows:

1) The reference image is rescaled and oriented to be roughly at the same scale and orientation as the signal image.

2) A small portion (15×15 pixels) of the signal image beginning with the upper left-hand corner is taken as a template pattern.

3) A two-dimensional cross correlation is performed between the template and the reference image.

4) The resulting cross-correlation coefficients are analyzed to determine the location of maximum correlation (1.0 for perfect correlation, -1.0 for anticorrelation). Any correlation values below 0.8 are rejected.

5) To obtain subpixel accuracy, the centroid of the eight neighboring cross-correlation coefficients is taken as the tie point location.

6) A new template is formed by shifting the 15×15 window by one pixel.

7) Steps 2–6 are repeated until the template has covered the entire image. This yields a set of tie points between the signal and reference images.

8) Steps 2–7 are repeated for all remaining images acquired in the preceding fashion.

9) An image transformation is determined in a least-squares fashion from the computed tie points.

10) The resulting image transformation is used to map the flat-field correction images to a common plane.

11) A flat-field calibration image (gain and offset) is produced from the calibration images.

12) The flat-field calibration is applied to each image, and steps 1–11 are repeated to remove any potential bias that might be associated with the separate imaging systems used to acquire each image.

This algorithm was implemented using MATLAB® software. Step 9 was performed using the MATLAB script function cp2tform, which computes an optimal (least-squares-based) image transformation based on the set of tie points defined between the two images. Steps 10–12 are necessary to remove any potential bias that might result from a nonuniform response of one image relative to the other. This was particularly a concern with the single-camera PDV system where the use of finite-size mirrors can produce intensity gradients across the images. In the current experiments, however, steps 10–12 had only a very minor and subtle effect on the optimum image transformation. Visually, the preceding procedure produced very accurate alignments between the two images that were similar to, if not better than, image alignments produced using the conventional dot-card approach.

The next step in data analysis is a calibration between the signal and reference images to ensure equal response by both imaging systems to the same input. This step is commonly called a "green card" or a flat-field correction and accounts for any differences in intensity between the signal and reference images that are not caused by Doppler shift. Sources of nonuniformity can include background absorption by the iodine filter, different optical paths, and pixel-to-pixel variations in CCD sensitivity. Two approaches are commonly used to achieve this goal. In the first approach, a white card is placed at the image plane, and laser light is directed onto the card through an optical diffuser, creating a smooth intensity field (thus, the term green card). Images are then taken with the laser tuned to maximum transmission, and the relationship between signal and reference image sensitivity can be determined. In the second approach, the

laser is also tuned to maximum transmission, but images are taken of the jet downstream of the jet core where velocities are lower.

To complement the image-alignment method outlined earlier, the second approach was used in these experiments. Instead of imaging a far downstream region of the jet, however, the jet was operated overexpanded as discussed. The advantage to using jet images for the calibration is that all experimental details remain the same between the calibration procedure and the actual data acquisition. The scattering particles, imaging plane (defined by the laser sheet), and background are identical between the calibration and experiment. A least-squares fit is then used to determine a gain (slope) and offset (intercept) value for each pixel location. For camera 1, it was found that each frame within a sequence of 28 frames had the same response. Thus, for the single-camera PDV experiment 24 sets of images (28 images per set) produced 672 signal and reference intensities at each pixel from which a gain and offset value could be determined. Camera 2 also appeared to have a uniform response over all 28 frames. The location of the dead pixels, however, varied from frame to frame. The pattern of dead pixels repeats itself every fourth frame, however. This is likely because of the 8×4 arrangement of memory modules next to each pixel. Thus, frames 1, 5, 9, 13, 17, 21, and 25 have the same response. Similarly frames 2, 6, 10, 14, 18, 22, and 26 are similar. Consequently, calibrations were determined separately for each grouping of frames. Twenty-nine sets of images were used for the two-camera PDV calibrations, resulting in gain and offset values determined from 203 (29 sets $\times$ 7 frames/grouping) intensity measurements.

Conventional methods of image alignment and calibration (dot cards and green cards) were also used. It was found to be difficult to precisely align the dot card or green card with the laser sheet in the current facility; the jet is mounted on a stand approximately 1.6 m above the ground and exhausts into an anechoic chamber. Even so, the conventional methods worked fairly well and produced good results. There is more confidence in the data using the preceding procedures, however. In addition, data were easier to acquire in this manner as the laser frequency and jet operating pressure could be adjusted quickly and effortlessly. In additions, this method will eliminate any errors that might be introduced by an imprecise alignment of the dot-card/green-card plane with the laser-sheet plane.

Once the image alignment and calibrations are performed, the experimental data can be processed to determine velocities. The procedure is straightforward. First, the images are loaded into MATLAB, background subtracted, and image transformation applied so that both images are mapped to the same plane. Before finding the ratio between the two images, one has the option of applying an image filter to remove any random noise that might be present in the raw images. The choice of filters varies widely and is largely a matter of preference. As will be discussed in more detail, the dominant form of noise in these experiments is speckle noise. Clancy et al.[25] experimented with different filter types and found that the use of homomorphic Wiener filter using the MATLAB script wiener2 removed significant portions of the speckle noise while preserving edges and geometrical shapes fairly well. This type of filter was compared with nonhomomorphic filters as well as other filter types (e.g., a 3×3 low-pass averaging filter). Thus, each image was treated with a 3×3 kernel homomorphic Wiener filter prior to data processing. An effect of image filtering, however, is a reduction in the measurement's spatial resolution. Thus, the effective resolution of the current measurements is approximately 2 mm for the single-camera experiment and 1.44 mm for the two-camera experiment.

Following image filtering, the calibration (gain and offset) was then applied to the images and the signal divided by the reference yielding a transmission ratio for each pixel location. For both the single- and two-camera setups, the laser frequency was set to yield a transmission ratio of approximately 0.9 (8.05 V on the left branch in Fig. 2). Consequently, lower velocities yielded a higher transmission ratio and high velocities a low transmission ratio. This scheme provided for a higher signal at the edges of the mixing layer where image intensities tended to be lower. A look-up table incorporating bicubic interpolation and the data from Fig. 2 were used to determine the corresponding frequency (given in volts and converted to frequency using 8.62 GHz/V) at each pixel location. The frequency monitoring system was used to determine the precise frequency of the laser during the experimental run. Thus, a frequency shift was determined, and the velocity could be determined from Eq. (1). If the reference intensity was below a set threshold (100 counts of single camera, 250 counts for two camera), the velocity was assumed to be zero for that pixel location.

IV. Results

Data were obtained for the ideally expanded, rectangular Mach 2.0 jet with both the single-camera and two-camera PDV systems. Forty image sequences were obtained using the single-camera PDV setup and 36 image sequences for the two-camera setup. Each image sequence consists of 28 frames of velocity data produced by the 28 laser pulses shown in Fig. 1. In general, the image quality was good for the first 20 frames where the pulse energy was above 5 mJ. Beyond that, the quality varied from image sequence to image sequence. Some of the data obtained using the megahertz-rate PDV system are now discussed.

Figure 7 shows two typical signal and reference images acquired with the two-camera PDV system. Flow is from left to right, and the jet is seeded with acetone that condensed upon expansion through the Mach 2.0 nozzle; water vapor from the ambient air, entrained into the jet, also condensed upon mixing to visualize the majority of the mixing layer. Figure 7a is the reference image acquired with camera 2, and Fig. 7b is the signal image acquired with camera 1. The illumination of the flow is clearly not uniform, and the effect of orientation of the laser sheet is evident (see Fig. 6). The dark horizontal line passing through the lower part of the flow in the

a)

b)

Fig. 7 Raw images acquired using the two-component PDV system: a) reference image from camera 2 and b) signal image from camera 1. Rectangle marks a large-scale structure within the mixing layer.

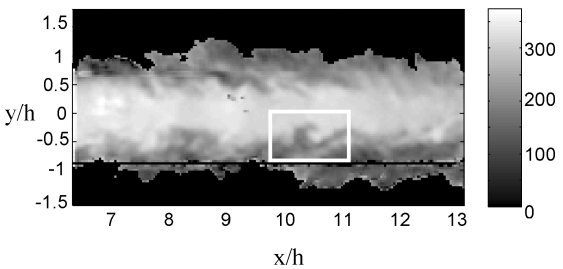

Fig. 8 Velocity image produced from signal and reference image of Fig. 7.

reference image is the result of some of the "dead" pixels on the CCD array that have not been accounted for by a postprocessing algorithm. The algorithm was designed to identify these regions of bad pixels and interpolate their values from neighboring pixels. Some of these regions, however, occur intermittently and are evident in some images. Even before image processing, the attenuation of the signal by the filter (velocity discrimination) is quite clear in the signal image. In general, higher intensities in the signal image correspond to lower velocities within the jet.

Figure 8 is a velocity image produced from the images of Fig. 7. A gray-scale map is used with lighter shades representing higher velocities. The velocity displayed is in the $0.68\,\boldsymbol{i} - 0.20\boldsymbol{j} + 0.71\,\boldsymbol{k}$ direction. Any intensity gradients apparent in the signal or reference images as a result of the nonuniform illumination have been removed in the PDV processing procedure, indicating accurate image alignment. Within the jet core, it is reasonable to assume that the $\boldsymbol{v}$ and $\boldsymbol{w}$ components of velocity are negligibly small. Along the centerline of the jet in Fig. 8, the measured velocity component is in the neighborhood of 340 m/s, which would correspond to an $\boldsymbol{u}$ component of approximately 500 m/s. For an ideally expanded Mach 2.0 jet, the centerline velocity would be approximately 505 m/s.

A number of features are present in Figs. 7 and 8 that could not be observed with simple flow visualization. Figure 7a is an example of how a typical flow-visualization image might appear. A box in this image marks the presence of what appears to be a large-scale structure with a fairly round body and thin braid regions upstream and downstream. The structure is observed by looking at the contrasts in intensity between the mixing layer and the jet core. This same region is highlighted in the velocity image of Fig. 8. In the velocity image (as well as the filtered image; Fig. 7b), the structure takes on a much more interesting appearance that cannot be discerned in the flow-visualization image alone. Rather, the structure shows a region of low-speed fluid that is wrapped, or rolled, up into the high-speed portion of the jet. This process is often shown in low-Reynolds-number and speed flows and is caused by the entrainment of ambient fluid into the jet.

The strength of megahertz-rate PDV, however, lies in its ability to obtain multiple images at sufficiently high frame rates to resolve dynamics of various scales in the flow. In this case, the frame rate is at 250 kHz, and there are 28 frames in the sequence that would yield more information about the entrainment process. Figure 9 shows an additional 21 frames of the flow and is zoomed into the region near the structure of interest. The contrast has been increased slightly to help aid in the visualization, although it can be difficult to follow the structure considering the limitations of the paper format. Viewing images in a top-to-bottom fashion, however, can assist the reader in visualizing the motion of this low-speed pocket of fluid as it is entrained into the jet. Over the sequence of frames, the

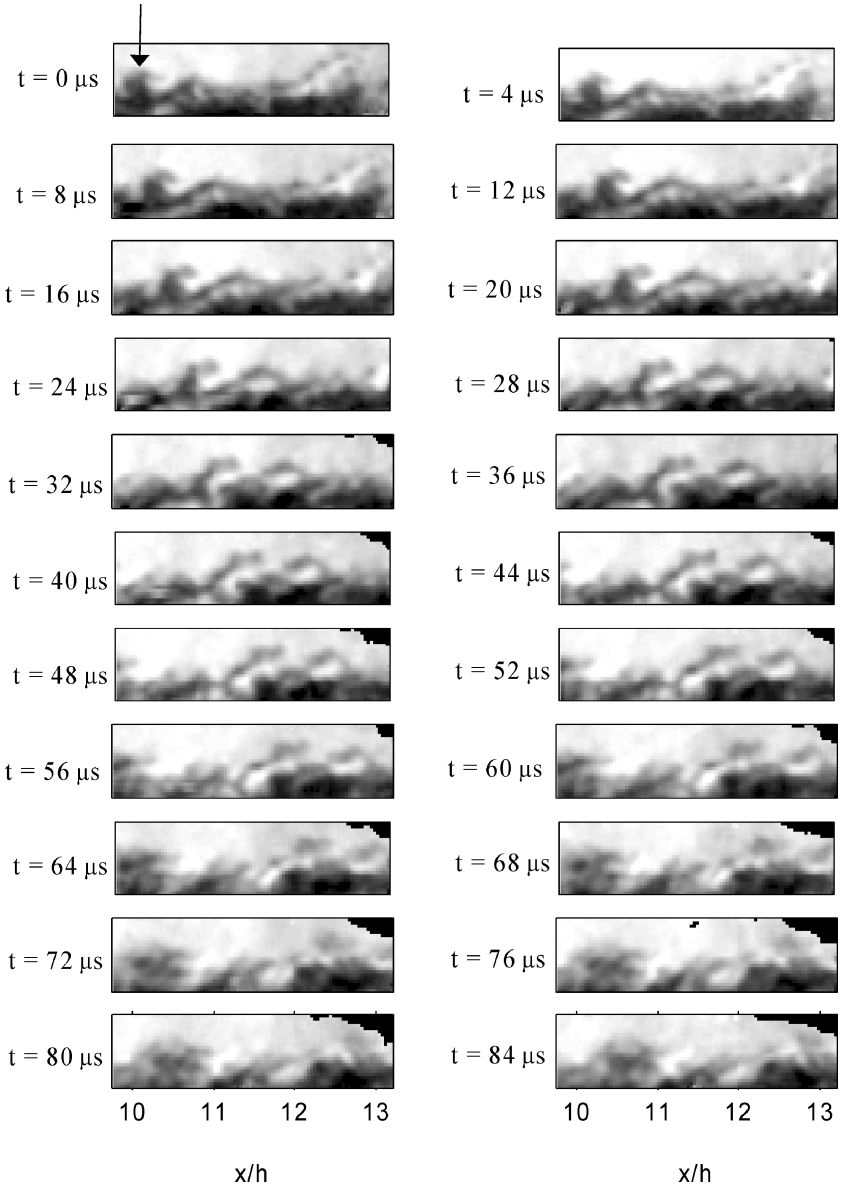

Fig. 9 Sequence of 22 velocity images depicting dynamic features of structure highlighted in Fig. 8. Data were acquired at 250 kHz.

low-speed fluid is pulled and stretched into the jet core. By the end of the sequence, the low-speed fluid can no longer be identified as its velocity has risen to the high speed of the surrounding fluid, and a clear contrast between high-speed and low-speed fluid is not present in this region. These 22 images depict the evolution of the shear layer over an approximate convective timescale of 3.5. The convective timescale is defined as $U_j * \Delta t/\delta$ with the shear layer thickness δ, defined as the distance from $U = 0.05$ to 0.95 U_{center} at $x/h = 10$. The entire sequence of 28 images covers approximately 4.5 convective timescales.

Clearly, a great deal of information is present in the acquired velocity data, and a number of quantitative methods exist (e.g., space-time cross correlations, proper orthogonal decomposition, etc.) to examine these data further. One must be cautious in the use of these data, however, as the measured velocity has an out-of-plane component. The planar images will not capture the out-of-plane motion of structures. A more complete picture can be obtained with the addition of other components of velocity. Recognizing this need, great emphasis was placed on obtaining data using a single camera. Obtaining accurate one-component data with a single camera will free up the use of a second camera to obtain a second component of velocity. Given the high cost of high-speed cameras, the significance of this cannot be understated.

As an example of the capabilities of the single-camera PDV experiment, Fig. 10 displays a 28-frame sequence of velocity images obtained using a single camera. Images are arranged left to right, top to bottom, and 4 μs separates each frame. As with the two-camera setup, the results are quite encouraging. In fact, as will be discussed, the accuracy of the single-camera setup is somewhat better than the two-camera system. The tradeoff, however, is a reduced field of view for the image sets. The entire set of 28 frames is included in Fig. 10 to emphasize the ability of the megahertz-rate PDV system to acquire data at high frame rates. Observing the images from top to bottom can aid the reader in following the motion of turbulence

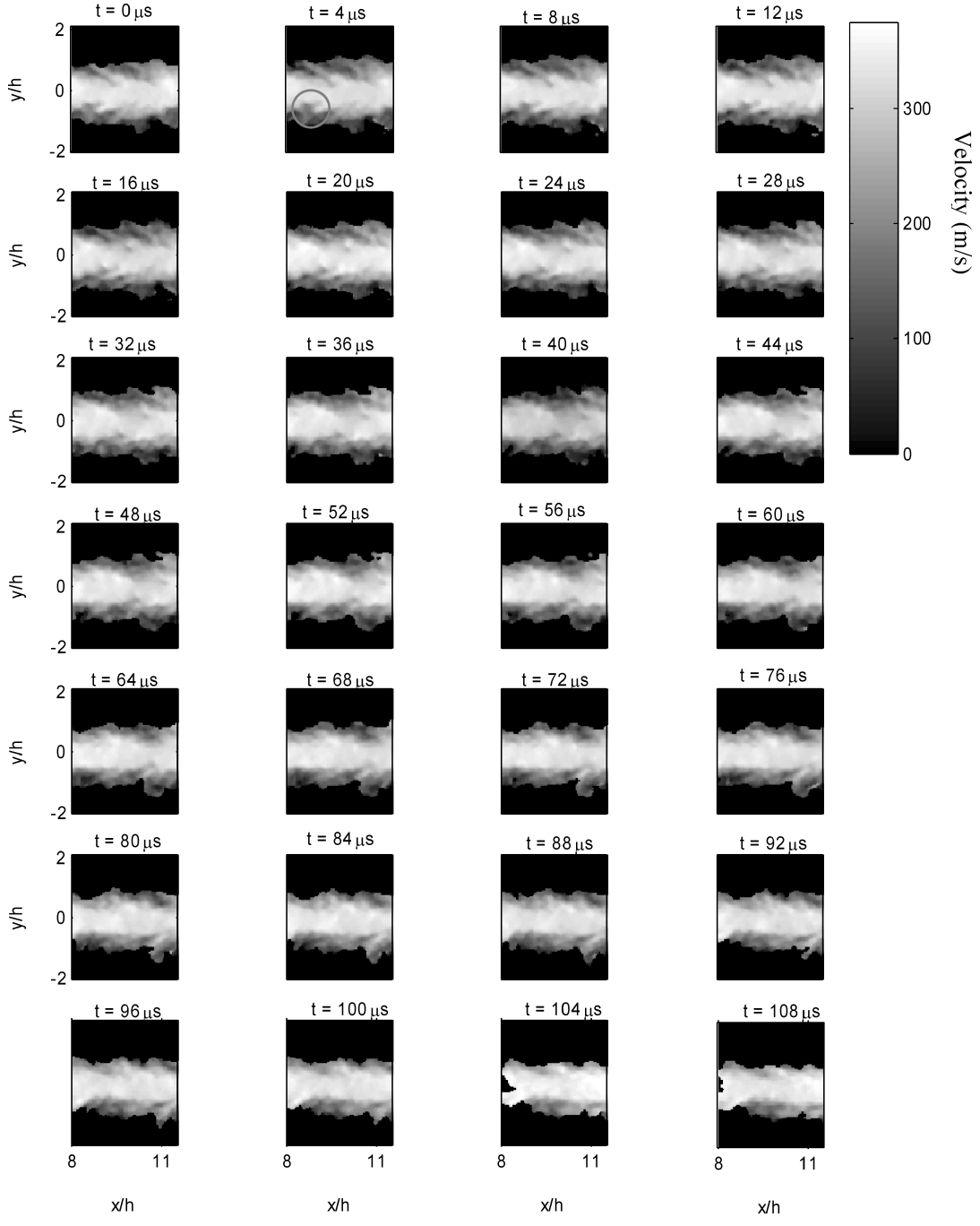

Fig. 10 Sequence of 28 velocity images of Mach 2.0 jet obtained with single-camera PDV setup. Data were acquired at 250 kHz.

structures across the image sequence. As an example, a circle in the second frame of the sequence highlights a patch of low-speed (darker shading) fluid that is pulled and stretched into the high-speed jet core. This appears to be similar to the process described earlier and depicted in Fig. 9.

Sufficient image sets were acquired to allow for the calculation of ensemble average flow and turbulence statistics. Only images that registered a velocity through the entire streamwise extent of the image were used in the calculations; images where the pulse energy or seeding level was not sufficient to illuminate the entire flowfield were not included. Figure 11 contains the average and fluctuating velocities for the single-camera experiment. A total of 819 frames from 40 image sequences were used. Figure 12 shows the corresponding images for the two-camera experiment. A total of 258 images from 36 image sequences were used.

The calculated statistics are expected to be slightly inaccurate for two reasons. First, the seeding technique used does not provide for seed particles in the still ambient air. Thus, there is a boundary at the outer edge of the mixing layer beyond which velocity measurements cannot be made. It is assumed that the velocity in the regions outside of the marked mixing layer is zero. Practically, however, these velocities can range from zero to up to 100 m/s (which seems to be the approximate cutoff velocity for the outer edge of the visualized mixing layer). Second, although a large number of images (819 and 258) were used, the images are time correlated because of the high frame rates involved. Consequently, standard statistical conventions cannot be applied.

In both figures, expected trends can be observed. In the average images, the velocity smoothly transitions from the high-speed jet core to the ambient fluid at rest. The fluctuating velocity images show a higher level of turbulence within the mixing layer and a low level of fluctuations within the jet core. The large levels of fluctuations in the upstream portion of the jet core in Fig. 12b) are the product of a region of dead pixels on the camera 2 CCD chip. Any measurements made in the immediate neighborhood of these damaged pixels are unreliable and become more evident in the rms images. Looking past these regions, the measurements appear to be quite good.

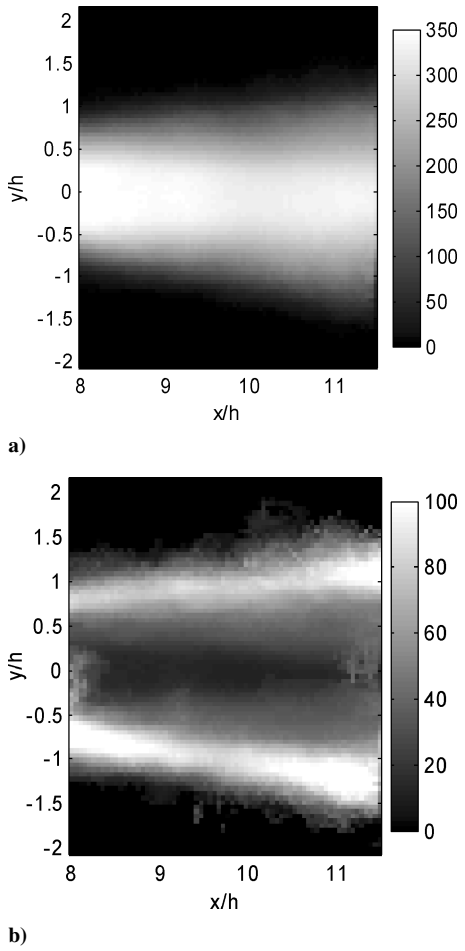

Fig. 11 Deviation velocity images obtained with single-camera PDV system: a) average and b) standard.

The statistical data allow for a comparison of the single-camera and the two-camera setups and an assessment of the repeatability and reliability of the experimental procedure as the experiments were conducted on separate days. Figure 13 is a graph of the ensemble-averaged velocity profiles at $x/h = 8$, 9, 10, and 11 for both the single-camera and two-camera data with each location offset by 100 m/s. The velocity profiles undergo the expected broadening with downstream distance reflecting the growth of the jet's mixing layer. The agreement of the profiles at each location is quite good. Some disagreement can be observed toward the outer edge of the mixing layer. This could be because of some of the reasons already discussed.

The average centerline velocity at $x/h = 8$ is approximately 360 m/s for both sets of data in the measured direction. This would correspond to an $\boldsymbol{u}$ component of approximately 529 m/s assuming $\boldsymbol{v} = \boldsymbol{w} = 0$. This is approximately 5% higher than the expected isentropic velocity of 505 m/s. In addition, velocity profiles along the jet centerline are marked by fluctuations on the order of 10–20 m/s that are not consistent with an ideally expanded jet. These trends might be the result of a number of items. Bias errors, to be discussed in the next section, are on the order of 12 m/s and can account for some of the observed trends. The agreement between the two independent measurements, however, for which the bias errors would be different, indicates that the measurements might indeed be accurate.

To further assess the general character of the studied Mach 2.0 jet, pitot measurements were conducted. In general, pitot measurements are useful in characterizing some of the gross features of a flowfield via mean velocity measurements. Thus, they are used here to identify key characteristics of the measured flowfield. Measurements along the jet centerline show the presence of a weak shock-cell pattern within the flowfield. Unfortunately, the nonideal operation of the jet could not be avoided in the current jet facility where pressures (at this operating condition) could only be set to within ± 1.0 psi. The rectangular geometry and thick lip of the nozzle also contribute to the nonideal behavior of the jet flow. The shock-cell spacing within the imaging region is similar to that measured with the PDV system and, assuming a static pressure of ambient, would cause a variation in centerline velocity on the order of approximately 10–20 m/s, consistent with that observed along the centerline in the PDV measurements. Transverse profile pitot measurements indicate a mixing-layer thickness very close to that measured with the PDV system. Thus, the pitot measurements were consistent with the PDV data and indicate good accuracy from the PDV system.

Figure 14 is a comparison of the velocity fluctuations at $x/h = 9$, 10, and 11. Again, the match between the two sets of data is quite good, particularly at the jet centerline. The larger number of images included (819 vs 258), higher accuracy, and a higher-quality CCD chip lead to a smoother turbulence profile for the single-camera data. Fluctuations in the jet core are approximately 3–5% of the average velocity. The same levels of fluctuation were observed in a Mach 2.0 axisymmetric jet by Clancy et al.[12] using both a three-component conventional PDV system and LDV measurements. In the shear layer, the velocity fluctuations peak at a approximately 20–25% of the jet core velocity. Measurements made by Clancy et al.[12] were at a location farther upstream, but of a similar magnitude (approximately 15%). The difference in flow geometry, downstream location, and also smaller sample size in the current work, which will tend to increase fluctuations level in the mixing layer, make direct comparison qualitative. The assumption of zero velocity outside of the mixing layer will lead to a slightly higher measurement of turbulence near the outer edges of the mixing layer. Still, the measurements are quite encouraging and help establish the accuracy of the technique.

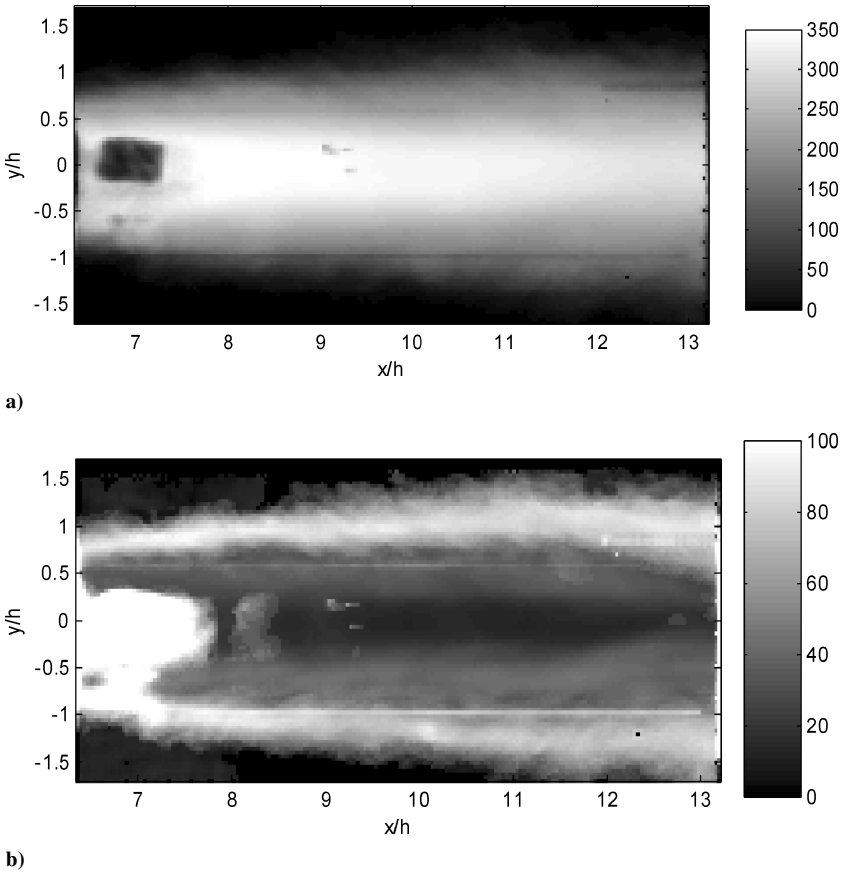

Fig. 12 Deviation velocity images obtained with two-camera PDV system: a) average and b) standard.

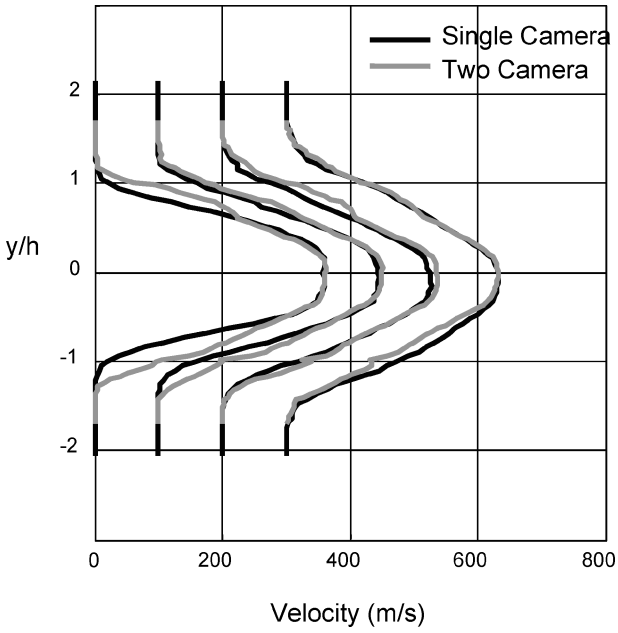

Fig. 13 Average velocity profiles taken at streamwise locations of $x/h = 8$, 9, 10, and 11. Each profile is shifted by 100 m/s.

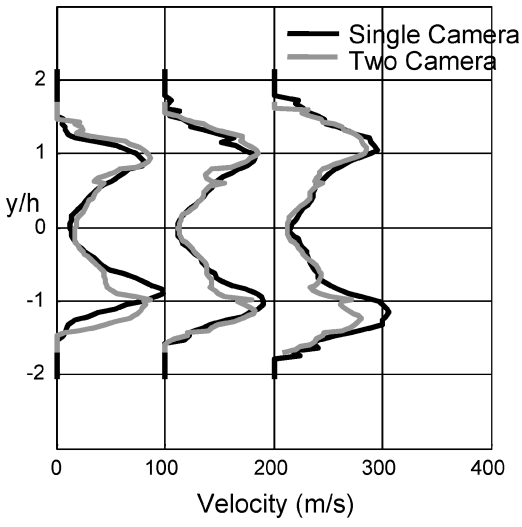

Fig. 14 Velocity fluctuation profiles taken at streamwise locations of $x/h = 9$, 10, and 11. Each profile is shifted by 100 m/s.

V. Error Analysis

Several investigators have performed comprehensive and detailed uncertainty analyses of PDV systems (e.g., McKenzie,[9] Elliott,[26] Elliott et al.,[7] Beutner et al.,[13] Clancy et al.,[12] and Smith[27]). This paper does not seek to repeat the comprehensive scope of these analyses, but rather will look at the foremost error sources that are pertinent in the application of the pulse burst laser and high-speed cameras.

Generally, error sources are categorized as either bias or random errors. Bias errors are constant from image to image and will not average out over large sets of data. Random errors, on the other hand, will vary from image to image, but will average out given sufficient number of images. Whether bias or random, noise can also take the form of fixed or multiplicative. For a fixed noise source, the amount of noise is independent of signal. The dominant form of noise in PDV systems, however, is of the multiplicative type. For this type of noise, it is easy to show

$$\sigma_{\mathrm{TR}} = \mathrm{TR} \times \sqrt{\mathrm{NSR}_S^2 + \mathrm{NSR}_R^2} \tag{2}$$

Table 2 Summary of estimated and measured error sources for single-camera PDV system

Type	Error source	TR 0.3	TR 0.5	TR 0.7
Bias errors	Angles	5	4	2
	Calibration	6	10	22
	Frequency jitter	5	5	5
Total bias		**9**	**12**	**22**
Random errors	Camera dark noise	2	2	2
	Speckle	9	15	32
Total random		**9**	**15**	**32**
Measured error (random)	Unfiltered	9	14	30
	3×3 filtered	3	5	11
Total error	Filtered (random and bias)	**10**	**13**	**25**
	% Centerline	2.8	3.7	7.1
	% Local	2.6	4.5	12.8

where σ_{TR} is the error in transmission ratio (TR) and NSR_S and NSR_R are the noise-to-signal ratio for the signal and reference images, respectively. For multiplicative noise, the noise becomes a function of the transmission ratio itself.

In addition, the conversion from TR to velocity is a nonlinear function. Consequently, the error in velocity will be a function of velocity and therefore transmission ratio. This fact will be important when considering the expected error within different regions of the jet. As such, errors are considered for TRs of 0.3, 0.5, and 0.7, corresponding to velocity measurements of 367, 285, and 193 m/s, effectively covering the range of velocities measured in this study. Table 2 is a list of various error sources and their estimated values at these different TRs. Only values for the single-camera experiment are reported in Table 2. The two-camera experiment produced similar results and is not discussed in detail for the sake of brevity and clarity. Each source will be discussed in the following. The error analysis is begun with a consideration of bias errors.

Some common sources of bias error include laser frequency uncertainty, imprecise image alignment and calibrations, and inaccurate measurement of the experimental setup (angle of incident and scatter light vectors). Unlike conventional pulsed Nd:YAG lasers, the frequency of the pulse burst laser is quite stable as discussed earlier. Frequency jitter of the pulse burst laser is not expected to be significant and was immeasurable because of the 12-MHz resolution of the frequency monitoring system. Frequency drift on the other hand could approach 50 MHz/h. The use of the frequency monitoring system, however, should eliminate this as a significant source of error. In addition, filter profiles were taken before and after each experiment to further monitor any drift. Without additional data to confirm the lack of frequency jitter within the pulse burst laser, a conservative estimate of 12 MHz will be used. This error is independent of the velocity and will produce an error of approximately 5 m/s.

The accuracy of the image alignment and calibration procedure is difficult to assess quantitatively. As discussed earlier, the alignment and calibration was determined by setting the pulse burst laser to full transmission and acquiring images of a highly overexpanded jet. Ideally, the signal and reference images would be identical using this procedure, and no attenuation should occur through the iodine filter. Realistically, however, the finite velocity of the particles in the flow producing the image will produce some Doppler shift. Analyzing the filter profile at the point of maximum transmission shows that the filtered intensity could be reduced by up to 5% for jet core velocities of 500 m/s (although expected to be much lower because of operation in the overexpanded regime). To err on the conservative side, a 5% error in gain is assumed and leads to bias errors ranging from 6 (TR = 0.3) to 22 m/s (TR = 0.7) depending on the flow velocity.

Any uncertainty in the measurement of the angle between incident and scattered light vectors will lead to a bias error that is proportional to the velocity. Assuming 2-deg accuracy, the bias error as a result of angle measurement is estimated to be from 2 to 5 m/s. Adding these three bias error sources in quadrature leads to a total estimated bias error of 9–22 m/s. The main source of inaccuracy is caused by the calibration procedure. This source of error can be significantly reduced by ensuring lower velocities of the jet within the imaging region. For example, a smoke generator can be used to provide small low-speed particles for light scattering.

Random error sources are of added importance in megahertz-rate PDV because of the time correlation between velocity images. Averaging out errors is not an option when trying to determine details about dynamic features in the flow. Two common sources of random error include camera noise and speckle noise. Camera noise is a combination of readout noise and dark charge. These were measured by taking images with the lens cap on and measuring the fluctuating signal. For the camera 1, this noise was approximately 3 counts and for camera 2, 20 counts. This error is constant regardless of signal level. For a relatively low signal level of 1000 counts and a transmission ratio of 0.5, this leads to an uncertainty of approximately 11 MHz or 6 m/s for the two-camera setup and 4 MHz or 2 m/s for the single-camera experiment. In addition, camera 2 is estimated to have additional inaccuracies as a result of the large number of damaged pixels on the CCD. Intensity readings in the vicinity of these damaged pixels are somewhat unreliable, and application of the image alignment and calibration in these areas is not straightforward. This additional component of noise was not quantified directly, but is suspected to be a significant source of error in the two-camera experiments.

Speckle noise is typically the most dominant noise source and a limiting factor in many PDV experiments. Speckle is the result of constructive and destructive interference produced by the scattered coherent laser light as it travels at slightly different path lengths from the scattering medium to the CCD chip. McKenzie[28] and Smith[27] characterized the noise-to-signal ratio (NSR) of speckle by

$$\mathrm{NSR} = 1.2(1 + m)\lambda F/\Delta x \tag{3}$$

where m is the magnification of the system, F is the lens f/#, and Δx is the average pixel size. For the single-camera experiment, the f/# is effectively doubled as only half of the lens is used to image the signal image, with the other half of the lens used for the reference image. Using Eq. (3), camera 1 will produce an NSR of 5.2% for each image. For the two-camera experiment, each lens is dedicated solely to the signal and reference images. In this case, camera 1 will produce an NSR of 2.6%, and camera 2 will produce an NSR of 4.5%. Speckle noise is multiplicative, and Eq. (2) applies. For the single-camera experiment, the expected error ranges from 9 (TR = 0.3) to 32 m/s (TR = 0.7) depending on the velocity. For the two-camera experiment, the error caused by speckle is expected to be slightly lower and in the range of 6–23 m/s. Speckle noise can be reduced, however, at the expense of measurement resolution using various image filters. In these experiments, a 3×3 homomorphic Wiener filter was used. This step effectively triples the size of each individual pixel, and one can expect error caused by speckle to decrease by approximately a factor of three.

The preceding error determination is only an estimate of the major sources of error and not a comprehensive analysis of all potential error sources. A better indication of accuracy can be obtained directly from the jet calibration images. Again, these images were acquired with the laser at full transmission, and the jet operated in the overexpanded regime. Ideally, the transmission ratio should be equal to 1.0 at every pixel in the ratioed image. Any random sources of error, however, will cause the measured ratio to vary from this value. The variation of these values from 1.0 can then be used to determine the random errors of the system. For all of the calibration images, a histogram of the calculated transmission ratios produced a Gaussian distribution. The level of fluctuations is calculated as the standard deviation of these values and considered to be the amount of random error for these experiments.

For the single-camera experiment and no image filtering, the variation was approximately 7%. The fluctuations varied from 5 to 8% depending on the signal level as well as the location within the image. In general, higher intensity regions of the image had slightly lower noise levels (because of higher signal levels). The measured fluctuations are assumed to be predominantly caused by multiplicative

noise sources such as speckle (the most dominant source of random noise), and thus Eq. (2) will apply. Taking 7% as the total NSR of the transmission ratio [square root of Eq. (2)] produces velocity errors ranging from 9 m/s (TR = 0.3) to 30 m/s (TR = 0.7). These values are extremely close to the random errors just calculated and consisted mostly of speckle. Thus, speckle is believed to be the limiting factor in these experiments. When image filtering is applied, the fluctuations reduced significantly to approximately 2–3%, correspondingly lowering the measured random error to 3–11 m/s. Similar results were observed for the two-camera experiment where the transmission ratio varied between 3 and 6% with image filtering. This corresponds to an error on the order of 6–19 m/s, which is slightly higher than the single-camera experiment. The preceding results are summarized in Table 2 for the single-camera experiment. The two-camera experiment produced similar results, with the measured error being slightly higher. The two-camera experiment, however, has the added noise as a result of the unreliable quality of camera 2 in the vicinity of damaged regions of pixels.

The error determined from the calibration images does not account for the bias errors just estimated, which must be included in the total error. Combining the measured random errors with image filtering with the estimated bias errors produces a total error of 10 m/s for TR = 0.3 and 25 m/s for TR = 0.7. These errors are quite good and lend to the credibility of the acquired data. In terms of percentages (relative to centerline velocity), the error is approximately 3% within the jet core and 7% at the outer edges of the mixing layer. For the two-camera experiment, total errors range from 11 to 29 m/s, or 3 to 8% of the jet core velocity, respectively.

VI. Conclusions

The results presented in this paper are quite encouraging and demonstrate the ability of the pulse burst laser and commercially available high-speed cameras to acquire time-resolved velocity data. In this work, a sequence of 28 velocity images was taken at 250,000 frames per second. The potential uses for this data are plentiful. In one set of images, the process of entrainment was explored as a small portion of low-speed fluid was wrapped and rolled up into the high-speed region of the Mach 2.0 jet. The fluid was subsequently stretched and pulled in the streamwise direction until its velocity rose to that of the surrounding fluid, thus completing the entrainment process. This limited analysis, however, is just the tip of the iceberg as many more details about these processes remain to be discovered. Certainly, the use of megahertz-rate PDV is a step towards future discoveries within compressible flowfields.

For example, one of the current problems associated with SCRAMJET engines is the ability to rapidly mix fuel with air over a short distance. This problem is made difficult because of the high flow speeds and low growth rate associated with compressible mixing layers. As discussed in the Introduction, experimental techniques suitable for investigating better methods of fuel/air mixing are quite limited. The present work clearly expands these capabilities. In addition, the role of computational fluid dynamics (CFD) in aerospace engineering is increasing. The accuracy and robustness of various models for compressible flows, however, are limited because of the lack of experimental data on which to base and compare turbulence models and the long computational time still required to fully resolve all of the scales in the flow. Megahertz-rate PDV, however, now presents a tool that can produce velocity data with which CFD researchers can compare and further develop their models.

The ability to expand the one-component technique presented in this paper to two-components is quite clear as the data obtained with the single-camera experiment was of high quality and good accuracy. The addition of a second single-camera system will give researchers the ability to measure two components of velocity at megahertz rates. Naturally, the addition of a third camera system will complete the picture allowing for the measurement of all three components of velocity. This type of information will allow for highly detailed studies of compressible flows and their related applications.

Acknowledgments

The authors thank Charles Tyler and Cam Carter of the U.S. Air Force Research Laboratory for lending their Princeton Scientific Instruments camera to us for these experiments. The first author thanks the Department of Defense for his National Defense Science and Engineering Graduate Fellowship. The earlier support from the National Science Foundation to acquire megahertz-rate imaging technology and the support of Innovative Scientific Solutions, Inc., as part of a Phase II SBIR subcontract ((U.S. Air Force Research Laboratory—Propulsion Directorate) are also acknowledged. Marc Blohm's assistance in the pitot measurements is acknowledged.

References

[1]Cummins, H. Z., Knable, M., and Yeh, Y., "Observation of Diffusion Broadening of Rayleigh Sscattered Light," *Physical Review Letters*, Vol. 12, No. 6, 1964, pp. 150–153.

[2]Yeh, Y., and Cummins, H., "Localized Fluid Flow Measurements with a He–Ne Laser Spectrometer," *Applied Physics Letters*, Vol. 4, No. 99, 1964, pp. 176–178.

[3]Adrian, R. J., "Laser Velocimetry," *Fluid Mechanics Measurements*, edited by R. Goldstein, Hemisphere, Washington, DC, 1983, pp. 155–244.

[4]Komine, H., and Brosnan, S., "Instantaneous, Three-Component, Doppler Global Velocimetry," *Laser Anemometry*, Vol. 1, Aug. 1991, pp. 273–277.

[5]Meyers, J., and Komine, H., "Doppler Global Velocimetry: A New Way to Look at Velocity," *Laser Anemometry*, Vol. 1, Aug. 1991, pp. 289–296.

[6]Miles, R., and Lempert, W., "Two-Dimensional Measurement of Density, Velocity, and Temperature of Turbulent Air Flows from UV Rayleigh Scattering," *Applied Physics B*, Vol. B51, No. 1, 1990, pp. 1–7.

[7]Elliott, G. S., Samimy, M., and Arnette, S. A., "A Molecular Filter Based Diagnostics in High-Speed Flows," *Experiments in Fluids*, Vol. 18, No. 99, 1994, pp. 107–118.

[8]Arnette, S. A., Samimy, M., and Elliott, G. S., "Two-Component Planar Doppler Velocimetry in the Compressible Tturbulent Boundary Layer," *Experiments in Fluids*, Vol. 24, No. 4, 1998, pp. 323–332.

[9]McKenzie, R. L., "Measurement Capabilities of Planar Doppler Velocimetry Using Pulsed Lasers," *Applied Optics*, Vol. 35, No. 6, 1996, pp. 948–964.

[10]Smith, M. W., Northam, G. B., and Dummond, J. P., "Application of Absorption Filter Planar Doppler Velocimetry to Sonic and Supersonic Jets," *AIAA Journal*, Vol. 34, No. 3, 1996, pp. 434–441.

[11]Clancy, P. S., and Samimy, M., "Two-Component Planar Doppler Velocimetry in High-Speed Flows," *AIAA Journal*, Vol. 35, No. 11, 1997, pp. 1729–1738.

[12]Clancy, P. S., Samimy, M., and Erskine, W. R., "Planar Doppler Velocimetry: Three-Component Velocimetry in Supersonic Jets," *AIAA Journal*, Vol. 37, No. 6, 1999, pp. 700–707.

[13]Beutner, T. J., Williams, G. W., Baust, H. D., Elliott, G. S., Crafton, J., and Carter, C.D., "Characterization and Applications of Doppler Global Velocimetry," AIAA Paper 98-2608, June 1998.

[14]Mosedale, A. D., Elliott, G. S., Carter, C. D., and Beutner, T. J., "Planar Doppler Velocimetry in a Large-Scale Facility," *AIAA Journal*, Vol. 38, No. 6, 2000, pp. 1010–1024.

[15]Crafton, J., Carter, C. D., and Elliott, G. S., "Three-Component Phase-Averaged Velocity Measurements of an Optically Perturbed Supersonic Jet Using Multi-Component Planar Doppler Velocimetry," *Measurement Science and Technology*, Vol. 12, No. 4, 2001, pp. 409–419.

[16]Elliott, G. S., and Beutner, T. J., "Molecular Filter Based Planar Doppler Velocimetry," *Progress in Aerospace Sciences*, Vol. 35, No. 8, 1999, pp. 799–845.

[17]Samimy, M., and Wernet, M. P., "Review of Planar Multiple-Component Velocimetry in High-Speed Flows," *AIAA Journal*, Vol. 38, No. 4, 2000, pp. 553–574.

[18]Lempert, W. R., Wu, P. F., Zhang, B., Miles, R. B., Lowrance, J. L., Mastracola, V., and Kosonocky, W. F., "Pulse-Burst Laser System for High Speed Flow Diagnostics," AIAA Paper 96-0500, Jan. 1996.

[19]Wu, P., Lempert, W. R., and Miles, R. B., "MHz Pulse-Burst Laser System and Visualization of Shock-Wave/Boundary-Layer Interaction in a Mach 2.5 Wind Tunnel," *AIAA Journal*, Vol. 38, No. 4, 2000, pp. 672–679.

[20]Thurow, B., Hileman, J., Lempert, W., and Samimy, M., "A Technique for Real-Time Visualization of Flow Structure in High-Speed Flows," *Physics of Fluids*, Vol. 14, No. 10, 2002, pp. 3449–3452.

[21]Thurow, B., Samimy, M., and Lempert, W., "Compressibility Effects on Turbulence Structures of Axisymmetric Mixing Layers," *Physics of Fluids*, Vol. 15, No. 6, 2003, pp. 1755–1765.

[22]Thurow, B., Hileman, J., Samimy, M., and Lempert, W., "Progress Towards a Real-Time Quantitative Measurement Technique for High Speed Flows," AIAA Paper 2001–2985, June 2001.

[23]Thurow, B., Hileman, J., Samimy, M., and Lempert, W., "Progress Towards Real-Time Planar Doppler Velocimetry," AIAA Paper 2003-0916, Jan. 2003.

[24]Elliott, G. S., Samimy, M., and Arnette, S. A., "Study of Compressible Mixing Layers Using Filtered Rayleigh Scattering Based Visualizations," *AIAA Journal*, Vol. 30, No. 10, 1992, pp. 2567–2569.

[25]Clancy, P. S., Samimy, M., and Erskine, W. R., "Planar Doppler Velocimetry: Three-Component Velocimetry in Supersonic Jets," AIAA Paper 98-0506, Jan. 1998.

[26]Elliott, G. S., "The Study of Compressible Free Shear Layers Using Laser Based Diagnostic Techniques," Ph.D. Dissertation, Dept. of Mechanical Engineering, Ohio State Univ., Columbus, OH, 1993.

[27]Smith, M. W., "The Reduction of Laser Speckle Noise in Planar Doppler Velocimetry Systems," AIAA Paper 98-2607, June 1998.

[28]McKenzie, R. L., "Planar Doppler Velocimetry Performance in Low-Speed Flows," AIAA Paper 97-0498, Jan. 1997.

J. Trolinger
Guest Editor